Advanced Composite Materials
Publication details, including instructions for authors and subscription information:
http://www.tandfonline.com/loi/tacm20

Simulation of debonding for skin/stiffener composite structures

Yoshinobu Shimamura , Yoshiharu Miyamoto , Akira Todoroki & Hideo Kobayashi

Version of record first published: 02 Apr 2012.

To cite this article: Yoshinobu Shimamura , Yoshiharu Miyamoto , Akira Todoroki & Hideo Kobayashi (2005): Simulation of debonding for skin/stiffener composite structures, Advanced Composite Materials, 14:1, 63-81

To link to this article: http://dx.doi.org/10.1163/1568551053297102

Adv. Composite Mater., Vol. 14, No. 1, pp. 63–81 (2005)

Also available online - www.vsppub.com

Simulation of debonding for skin/stiffener composite structures

YOSHINOBU SHIMAMURA *, YOSHIHARU MIYAMOTO, AKIRA TODOROKI and HIDEO KOBAYASHI

Department of Mechanical Sciences and Engineering, Tokyo Institute of Technology, 2-12-1 O-okayama, Meguro, Tokyo 152-8552, Japan

Received 2 July 2004; accepted 1 October 2004

Abstract—Skin/stiffener composite structures suffer debonding between stiffener and skin due to loading. Application of fracture mechanics to assess structural integrity is difficult because of the complexity of structural configuration and inhomogeneity of composite materials. A simulation method to assess the structural integrity that predicts the onset and growth of debonding and estimates the stiffness degradation due to debonding is needed.

In this study, a simulation method based on FEM is investigated for skin/stiffener structures. The simulation method is intended to be versatile and easy to implement for commercial FEM codes. Skin/stiffener structures are modeled as coupling of shell elements. If debonding is judged by an energy criterion, the coupling is released. Debonding growth of Double Cantilever Beam (DCB) and End Loaded Split (ELS) specimens are simulated and compared with theoretical and experimental results to demonstrate the feasibility. Debonding of skin/stiffener structures is simulated successfully by the proposed method.

Keywords: Skin/stiffener structure; debonding; simulation; FEM.

1. INTRODUCTION

Carbon fiber reinforced plastic (CFRP) composites have been applied to aerospace vehicles because of their high specific modulus and strength. Recent progress in manufacturing methods enables us to fabricate integrated composite structures such as skin-stiffener structures [1], and thus to reduce the number of components. The skin-stiffener composite structures suffer debonding between skin and stiffener due to loading [2–5]. In order to estimate the structural integrity of the skin-stiffener structures, the onset and growth of debonding and the stiffness degradation of the structures due to debonding should be predicted. It is difficult to estimate the

*To whom correspondence should be addressed. E-mail: yshimamu@ginza.mes.titech.ac.jp

structural integrity because the structural shape and damage mechanics of CFRP are both complex. Recently, fracture simulation methods based on FEM have been developed. There are two objectives for these studies: micro-scale fracture simulation and structural-level fracture simulation. The latter is useful to estimate the structural integrity.

Most of the structural-level fracture simulation methods incorporate only intralaminar fractures, such as matrix cracking. Several researchers have reported simulation methods to deal with delamination and debonding. In order to simulate delamination and debonding, modeling by three-dimensional solid element is ideal. However, this is not practical due to the time needed to build such a model, the limit in computer resources and the necessary computation time. Several simplified methods have been proposed to solve these research aims. For example, a quasi-three-dimensional model and a new element that can handle debonding have been investigated [6–12]. In order to conduct a structural-level simulation, Shimamura *et al.* [6] used stiffness degradation equivalent to debonding, Zako *et al.* [7] used three-dimensional beam elements, and Majima *et al.* [8] developed an interface element. These studies are appropriate to simulate free-edge debonding and debonding by indent, but not appropriate to simulate debonding in complex shaped structures. Phillips *et al.* [13] reported a simulation method using an interface element for debonding of skin/stiffener structures. This method, however, needs a new element and special coding. For practical use, a simplified simulation method applicable to commercial finite element codes is desirable.

In this study, a method to simulate debonding of skin/stiffener structures is proposed to simulate the onset and growth of debonding, and to predict the stiffness degradation of the structure due to debonding. The method is applicable to commercial finite element codes on a PC with practical computer resources. Conventional shell elements are used to model skin/stiffener structures, and the energy release rate at a crack front is calculated to judge the onset and growth of debonding between skin and stiffener. The combination of shell elements and energy criterion may eliminate detailed analysis in the through-thickness direction. This approach may save computer resources and computation time, while maintaining sufficient accuracy. In order to demonstrate the feasibility of the proposed method, debonding of beam specimens and skin/stiffener specimens is simulated, and compared with experimental results.

2. SIMULATION METHOD

2.1. Modeling of skin/stiffener structure

In this study, debonding between skin and stiffener of skin/stiffener structures is investigated. Modeling of the skin/stiffener structures is as follows:

(i) Skin and stiffener are modeled by shell elements. Mesh division of adhesion areas must be same.

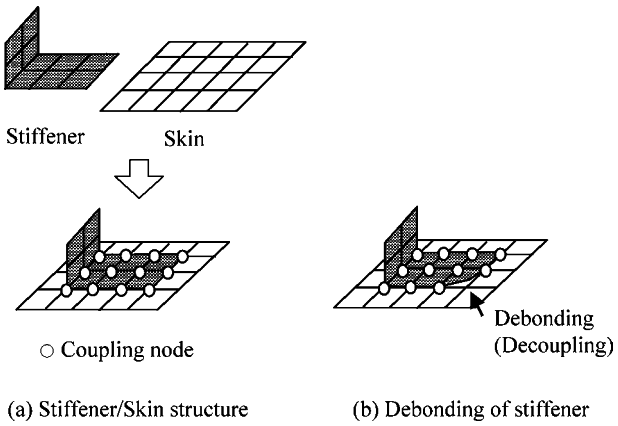

Figure 1. Modeling and debonding of skin/stiffener structure.

(ii) Adhesion is modeled by couplings of nodes whose coordinates are the same.

(iii) Debonding is modeled as decoupling of nodes.

Figure 1 shows the concept of modeling. There is no adhesive layer between skin and stiffener in this modeling, but it is possible to take account of the influence of an adhesion layer in a simulation routine of debonding judgment.

The assumptions made in this study are as follows:

(i) Composite laminates are regarded as homogeneous anisotropic laminates. First-order shear laminated shell elements are used in finite element analysis.

(ii) For simplicity, other fracture modes besides debonding are not incorporated.

(iii) Debonding occurs and propagates between skin and stiffener.

(iv) Onset and growth of debonding are regarded as the same phenomena.

(v) Energy criterion, i.e. the energy release rate, is used to judge debonding.

In order to save time to model skin/stiffener structures, computer resources and computation time, first-order shear laminated shell elements are used instead of three-dimensional solid elements. The shell element cannot analyze stress in the through-thickness direction, so an energy criterion is used to judge debonding.

In this study, a commercial finite element analysis code, ANSYS, was used for the solver. The simulation system is programmed using APDL, which is a macro programming language of ANSYS. Laminated shell element Shell 99 was used for modeling of the skin/stiffener structures.

2.2. Increment of debonding area

In this study, debonding is modeled by decoupling of nodes. The increment of debonding area dA depends on the shape of the crack front. The shape of the crack front should be classified to define the increment of debonding area to calculate the energy release rate.

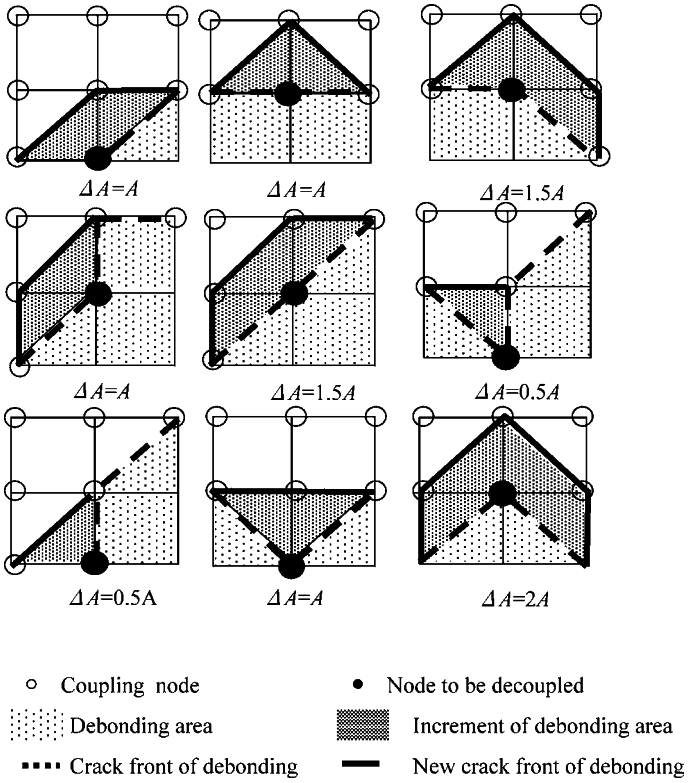

Figure 2. Increment of debonding area.

Figure 2 shows the classification of the shape of the crack front and the increment of debonding area in the case of square elements. In Fig. 2, the light gray area represents current debonding area, open and solid circles are coupled nodes, and the broken line is the edge of debonding. The dark gray area represents the increment of debonding area if a node shown by a solid circle is decoupled. The new crack front is represented by a solid line.

In the simulation routine, the increment of debonding area is calculated by searching the coupling status of nodes around the node to be decoupled and comparing to a database, like Fig. 2. If both square and triangular elements are used, the classification is more complex, but the increment of debonding area can be defined by the mesh division and the shape of crack front. In this study, only square elements are used to save computation time because the objective of this study is to demonstrate the feasibility of the simulation method.

2.3. Energy release rate

The virtual crack closure method [14] is used to calculate the energy release rate for all nodes that can be decoupled in the next step. It is virtually impossible to take strict account of the onset of debonding. Thus, initial infinitesimal cracks are

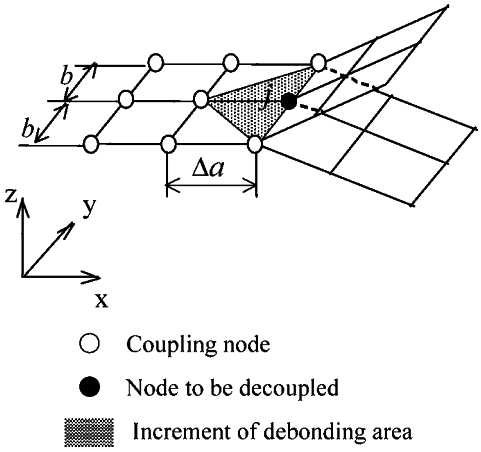

Figure 3. Model of coupled shell elements.

assumed to exist at the adhesive edge of skin/stiffener, and the virtual crack closure method is used to calculate the energy release rate.

The energy release rate at node j in Fig. 3 is described as follows:

$$\begin{aligned} G_{\mathrm{I}}|_j &= \frac{1}{2\Delta A}\left[F_{zj}(w_j - w'_j) + M_{xj}(\theta_{xj} - \theta'_{xj}) + M_{yj}(\theta_{yj} - \theta'_{yj})\right], \\ G_{\mathrm{II}}|_j &= \frac{1}{2\Delta A}\left[F_{xj}(u_j - u'_j)\right], \\ G_{\mathrm{III}}|_j &= \frac{1}{2\Delta A}\left[F_{yj}(v_j - v'_j) + M_{zj}(\theta_{zj} - \theta'_{zj})\right], \\ G_{\mathrm{T}}|_j &= G_{\mathrm{I}}|_j + G_{\mathrm{II}}|_j + G_{\mathrm{III}}|_j, \end{aligned} \tag{1}$$

where ΔA is the increment of debonding area, F_{xj}, F_{yj} and F_{zj} are respectively the nodal force in the x, y and z direction; M_{xj}, M_{yj} and M_{zj} are respectively the moment around the x, y and z axes; $(u_j - u'_j)$, $(v_j - v'_j)$ and $(w_j - w'_j)$ are respectively the nodal displacement in the x, y and z direction, and $(\theta_{xj} - \theta'_{xj})$, $(\theta_{yj} - \theta'_{yj})$ and $(\theta_{yj} - \theta'_{yj})$ are respectively the rotational angles around the x, y and z axes.

2.4. Judgment of debonding

The onset and growth of debonding is judged by an energy criterion. In this study, an energy criterion that takes account of all modal components G_{I}, G_{II} and G_{III} is adopted.

$$\frac{G_{\mathrm{I}}}{G_{\mathrm{Ic}}} + \frac{G_{\mathrm{II}}}{G_{\mathrm{IIc}}} + \frac{G_{\mathrm{III}}}{G_{\mathrm{IIIc}}} \geqslant 1 \tag{2}$$

where subscript c represents the critical energy release rate. In the simulation, the following simplified criterion is used because it is difficult to measure the

critical energy release rate G_{III} to separate mode III from mode II if the edge shape is complex. $G_{IIc} = G_{IIIc}$ is assumed to derive the following equation from equation (2).

$$\frac{G_I}{G_{Ic}} + \frac{G_{II} + G_{III}}{G_{IIc}} \geqslant 1 \tag{2'}$$

2.5. *Simulation flow*

The flowchart of simulation is shown in Fig. 4. The flow is basically the same as a conventional simulation method for intralaminar fractures [15]. First, the energy release rates at nodes of crack front and the adhesive edge of skin are calculated for a given applied load. By using Yamada's method [16], the most fragile node is judged and the fractional ratio of the applied load are calculated when decoupling occurs. By iterating the process one by one until the fractional ratio reaches 1, the debonding growth and the nonlinear load-displacement relationship are calculated.

The direct iteration method [17] is used to analyze the nonlinear load–displacement relationship. The advantage of the direct iteration method is that first derivative discontinuity of the load–displacement is allowed without any special algorithm. In other words, the direct iteration method is appropriate for fracture simulation. The advantage of Yamada's method is that the load increment is automatically calculated in the algorithm. Thus, the sole parameter that relates to convergence of the simulation result is mesh size. The influence of the mesh size will be discussed in Section 4.2. The disadvantage of the direct iteration method is that, in general, the method is not implemented in commercially available FEM codes. A routine to judge debonding must also be programmed externally. In our study, the direct iteration method and the routine to judge debonding were programmed by using APDL.

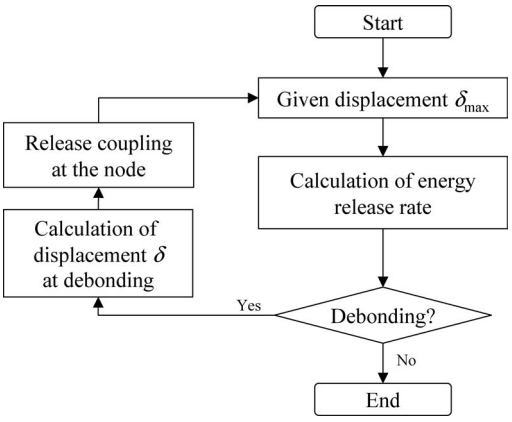

Figure 4. Flow chart of simulation.

In the proposed simulation method, required data are the finite element model of the skin/stiffener structure and material properties, i.e. elastic modulus and the critical energy release rate. The former is easy to build from CAD data, and the latter is easy to obtain from coupon tests. The proposed method is versatile, simple and practical.

3. DEBONDING OF BEAM SPECIMEN

In order to verify the simulation method, debonding of a CFRP plain-weave Double Cantilever Beam (DCB) specimen and End Loaded Split (ELS) specimen, as shown in Fig. 5, was simulated and compared with theoretical and experimental results. Debonding propagates one dimensionally for both specimens. DCB testing is pure mode I debonding and ELS testing is mixed mode (mode I + mode II) debonding.

3.1. Beam theory

Euler's assumption and linear beam theory were used to calculate the compliance of the beam and the energy release rate. A beam with width b, length L and height h has a pre-crack in the midplane whose length is a. A concentrated force is applied at the end of the specimen.

The energy release rate of mode I for the DCB specimen is described as follows:

$$G_I = \frac{12F^2a^2}{E_{11}b^2H^3}, \tag{3}$$

where A is the area of debonding, $H = h/2$, and E_{11} is the longitudinal modulus.

The energy release rate of mode I and mode II for ELS specimen are described as follows:

$$\begin{aligned} G_{\mathrm{I}} &= \frac{3F^2a^2}{E_{11}b^2H^3} \\ G_{\mathrm{II}} &= \frac{9F^2a^2}{4E_{11}b^2H^3} \end{aligned} \tag{4}$$

The ratio of mode I and mode II $G_{\mathrm{II}}/G_{\mathrm{I}}$ is independent of the crack length and equals 3/4.

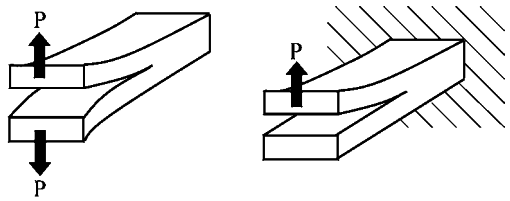

(a) DCB specimen (b) Mixed mode specimen

Figure 5. Beam specimens.

3.2. Specimen and experimental method

Four layers of CFRP plain-weave crossply prepreg (Mitsubishi Rayon Co. TR3110M) were laminated and cured by a hot-press. Rectangular plates were cut and adhered to fabricate DCB and ELS specimens. Figure 6 shows the specimen configuration and size. The process of adhesion is as follows: The surface of the rectangular plates were rasped by sand papers (#600), and the two plates were adhered by using room temperature curing epoxy resin (KOKUSAI Chemical Z-2/H-1) while a Teflon sheet was inserted to prevent adhesion of the pre-crack area. After curing, the Teflon sheet was removed, and the crack was propagated about 5 mm by using a wedge to make a sharp crack tip. Two specimens were prepared for both DCB and ELS testings.

The load was applied by a testing machine (Shimadzu AGS-1kN) under displacement control with a cross-head speed of 1.0 mm/min. The load–displacement relationship was monitored during testing. The crack length of DCB specimens was

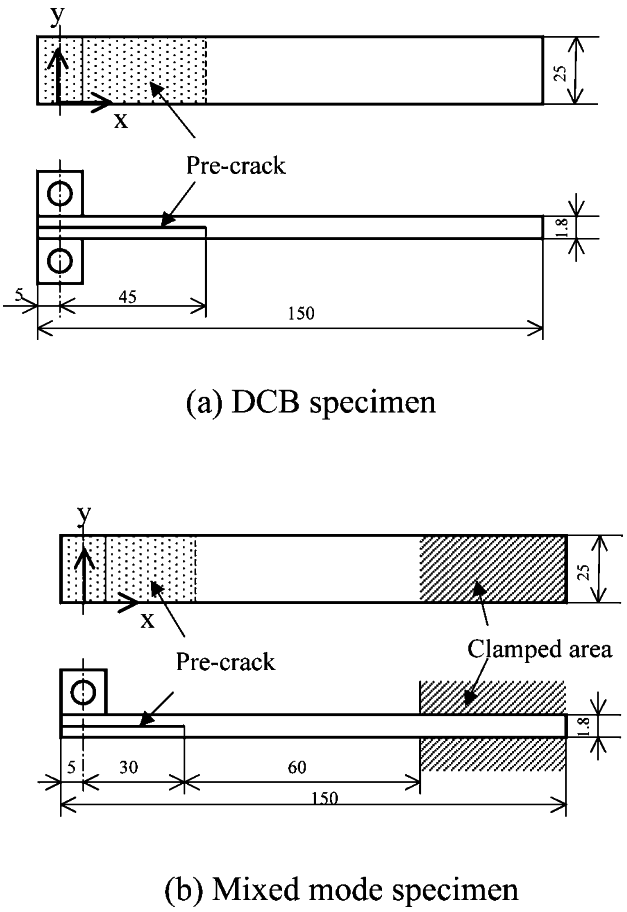

Figure 6. Configuration of beam specimens.

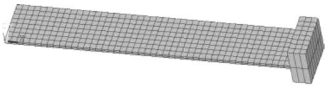

(a) DCB specimen

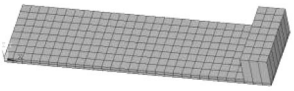

(b) Mixed mode specimen

Figure 7. FEM model of beam specimens.

Table 1.
Material properties of CFRP plain weave lamina

E_{11}, E_{22} (GPa)	E_{33} (GPa)	G_{12} (GPa)	G_{13}, G_{23} (GPa)	ν_{12}	ν_{13}, ν_{23}	G_{Ic} (J/m^2)	G_{IIc} (J/m^2)
50	7	5	3	0.3	0.45	91.9	170.2

measured by a microscope during testing. The crack length of ELS was estimated from the compliance of the specimen.

3.3. Simulation

FEM models are shown in Fig. 7. Material properties used in the analysis are shown in Table 1. Longitudinal modulus E_{11}, Poisson ratio ν_{12}, and fracture toughness G_{Ic} and G_{IIc} are experimental results, and other properties were based on references.

The energy release rate was calculated for all nodes of the crack front. Thus, while the shape of the crack front for theoretical analyses is assumed to be a straight line, the shape of the crack front for simulation is not always a straight line.

3.4. Results and discussion

Figure 8 shows the load–displacement relationship. The vertical axis is load and the horizontal axis is displacement. In Fig. 8, a solid line represents simulation, a broken line represents theory, and a dotted line represents experimental results. Figure 9 shows the increment of debonding. The vertical axis is the increment of debonding and the horizontal axis is displacement. In Fig. 9, a solid line represents simulation, a broken line represents theory, and symbols represent experimental results. The increment of debonding was defined as the length at a lateral edge.

For DCB testing, after reaching the maximum load, the load decreased gradually in accordance with debonding growth. A saw-shaped load–displacement relation-

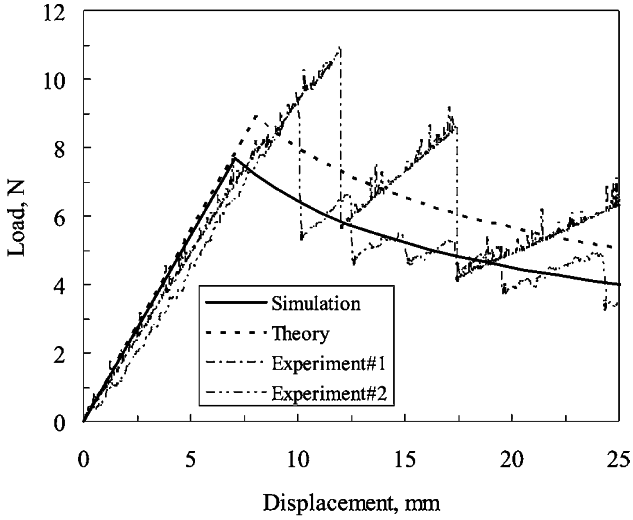

(a) DCB specimen

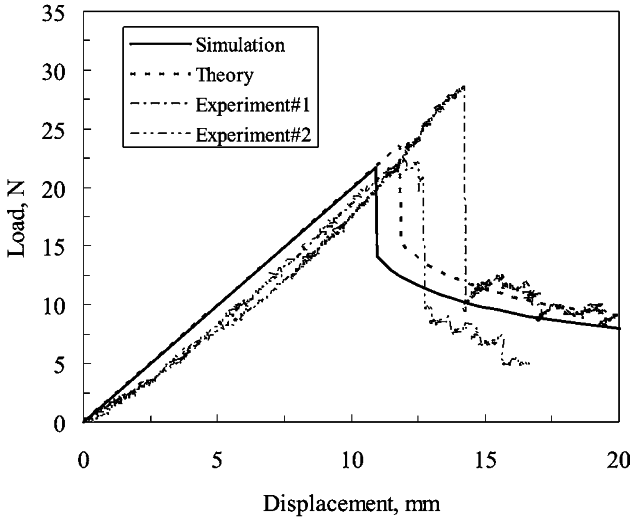

(b) Mixed mode specimen

Figure 8. Load *versus* displacement relationships.

ship was observed for experimental results. Two plain-weave laminates were adhered to make specimens, so the surface of the adhesive area was not flat and the thickness of the adhesive layer was uneven. This is because a so-called stick-slip phenomenon [19] occurred. The load–displacement relationship and the increment of debonding area in experiments showed agreement with theoretical and simulation results. It is shown that debonding growth in the DCB specimen can be simulated

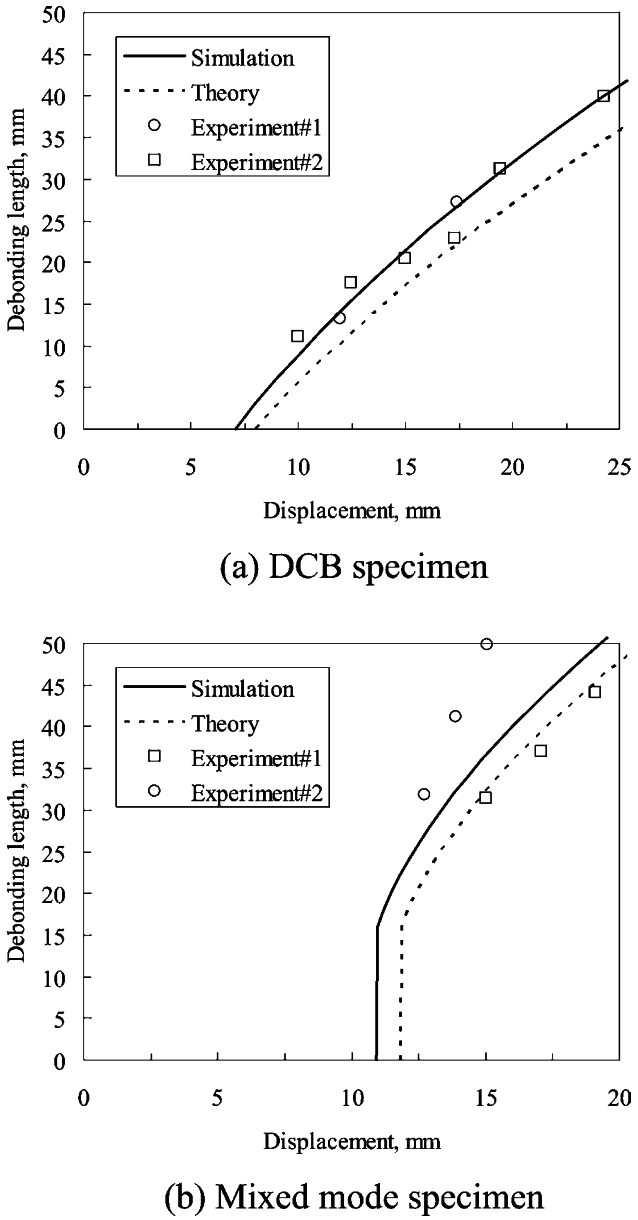

Figure 9. Debonding length.

by the proposed method. In simulation, debonding propagated faster than theory because the energy release rate at the crack front distributes. Figure 10a shows the distribution of the energy release rate at the crack front. The vertical axis is the energy release rate normalized by the theoretical value, and the horizontal axis is the y-coordinate normalized by the specimen width b. The energy release rate at the

center was larger than the theoretical value and this contributed to fast debonding growth.

For ELS testing, after reaching the maximum load, a rapid decrease of the load was observed in accordance with abrupt debonding growth of about 15–

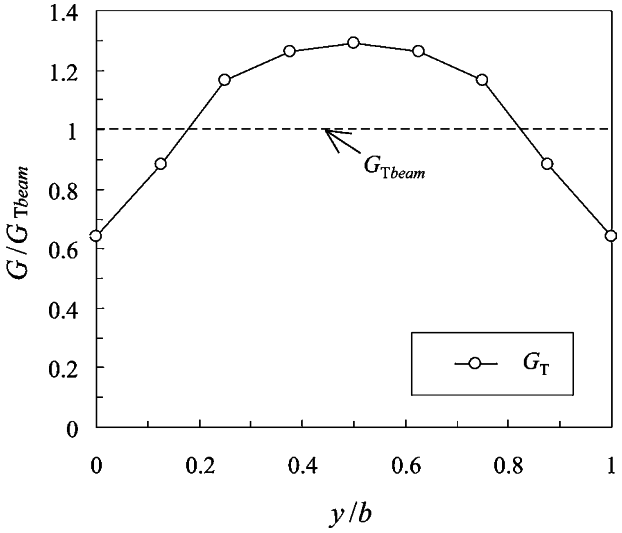

(a) DCB specimen

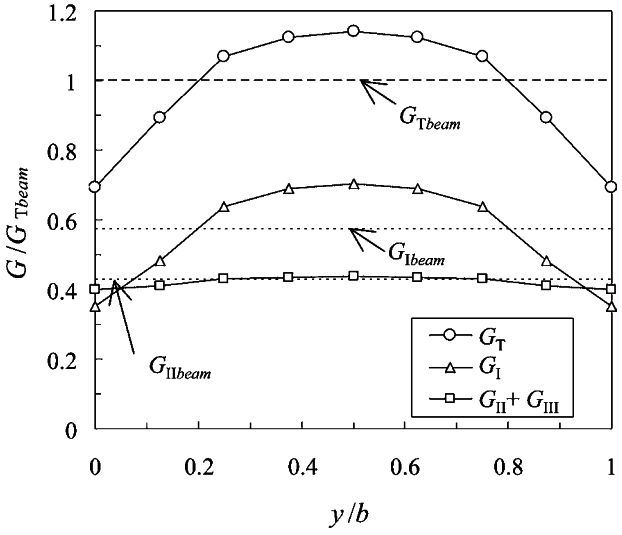

(b) Mixed mode specimen

Figure 10. Distribution of energy release rate.

30 mm. Then, the load decreased gradually in accordance with debonding growth. The load–displacement relationship and the increment of debonding in simulation agreed with theory and experimental results. In simulation, debonding propagated faster than theory because the energy release rate at the crack front distributed. Figure 10b shows the distribution of the mode I, mode II and total energy release rates at the crack front.

As a result, it is shown that the proposed method can simulate debonding growth in DCB and ELS testing. In other words, the proposed method can simulate debonding growth of not only pure mode I but also mixed mode.

4. DEBONDING OF SKIN/STIFFENER STRUCTURE

In order to demonstrate the feasibility of the simulation method, debonding of skin/stiffener structures were simulated and compared with experimental results. A plate with a stiffener was used as a specimen. Four specimens were prepared with a different orientation of the stiffener and position of loading. The points of interest are the ability to simulate the process and shape of debonding and the load–displacement relationship.

4.1. Specimen and experimental method

The material was the same CFRP plain-weave prepreg used for the beam specimens. The specimen was a plate with an L-shaped angle as shown in Fig. 11. One edge of the plate was clamped and a concentrated force was applied to induce debonding. The load–displacement relationship was measured during testing. The position of the blade of the L-shaped angle was parallel or transverse to the clamped edge. The position of the applied force was either in the center of the free edge opposite to the clamped one to apply mainly bending or near the corner of the free edge to

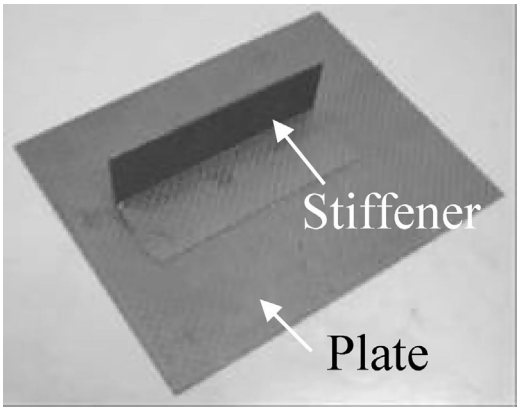

Figure 11. Photograph of skin/stiffener specimen.

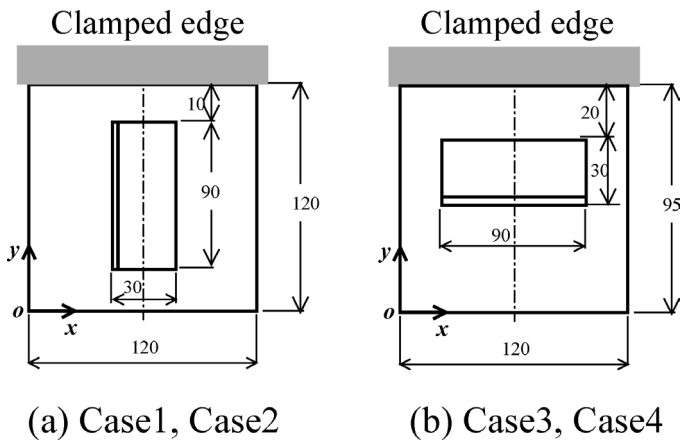

Figure 12. Configuration of skin/stiffener specimens.

Table 2.
Loading point

	x (mm)	y (mm)
Case 1	60	10
Case 2	15	15
Case 3	60	15
Case 4	15	15

apply bending and torsion. The specimen configuration is shown in Fig. 12 and the positions of the applied load are shown in Table 2.

The process to fabricate the specimen was similar to the beam specimens, but there was no pre-crack. Extra adhesive of the stiffener edge was removed carefully before curing in order to eliminate the influence of the adhesive at the edge. Three specimens were fabricated to measure the load–displacement relationship, and another one specimen was fabricated to measure the debonding shape. Load was applied by a testing machine (Shimadzu AGS-1kN) under displacement control with a cross-head speed of 2.0 mm/min. The load–displacement relationship was monitored during testing. The debonding shape was measured by an ultrasonic inspection (Hitachi Construction Machinery AT-5000).

4.2. Results and discussion

The analytical model used in the simulation is shown in Fig. 13. Arrows represent the position of loading. Material properties were the same as the beam specimens and shown in Table 1. Geometrical nonlinearity was considered in finite element analysis.

The load–displacement relationship is shown in Fig. 14 where the vertical axis is load and the horizontal axis is displacement. In Fig. 14, a solid line is

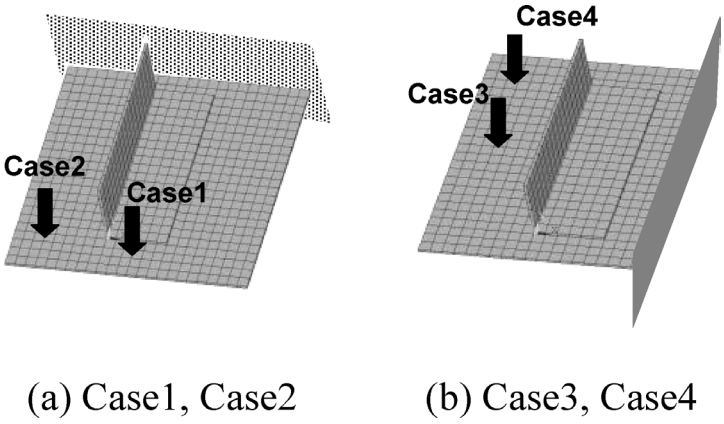

Figure 13. FEM model of skin/stiffener specimens.

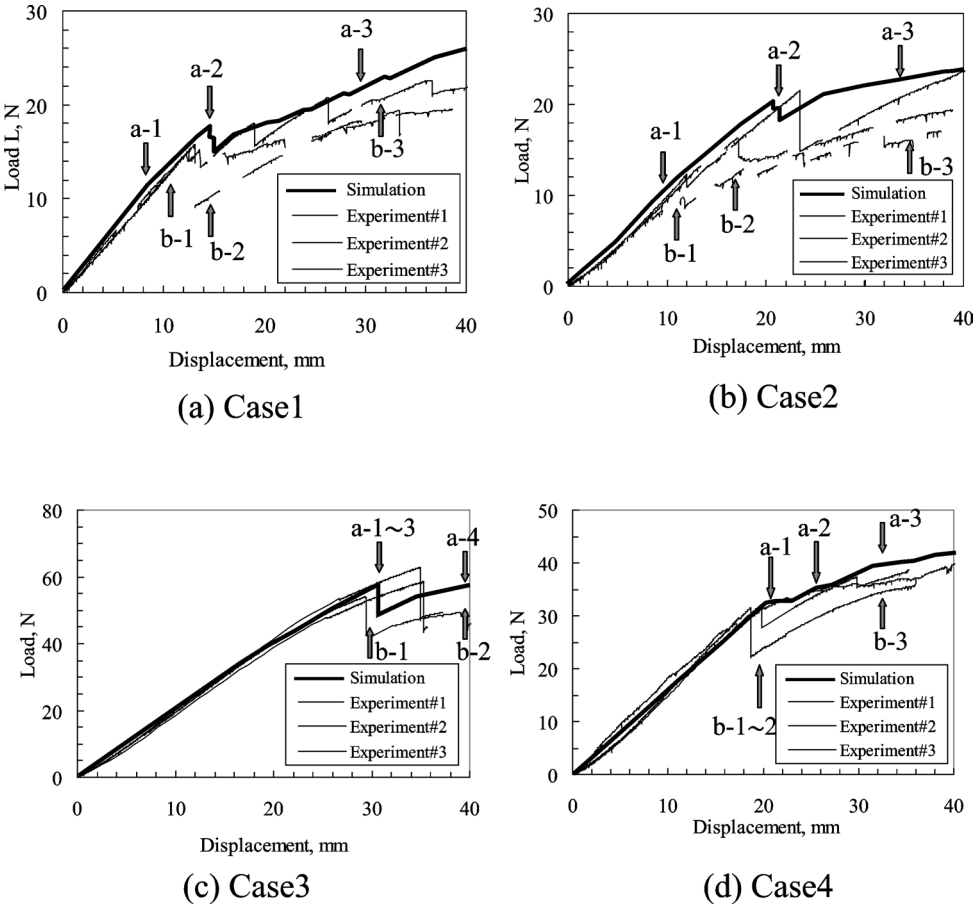

Figure 14. Load *versus* displacement relationships.

simulation and a broken line is the experimental results. The process of debonding growth by both simulation and C-scan is shown in Fig. 15. Arrows in Fig. 14 shows the displacements corresponding to each figure in Fig. 15. In experiments, the load–displacement relationships of three specimens had scattering because of unevenness of the adhesion layer and the influence of the adhesion edge. Note that the specimen for C-scan was different from specimens to measure the load–displacement relationship.

4.2.1. Case 1: Transverse stiffened and bending loading. Debonding occurred at the root of the blade near the clamped edge and then propagated to the transverse direction of the stiffener. After debonding reached the opposite side, debonding propagated abruptly about 20 mm, i.e. 1/4 of the stiffener length in the longitudinal direction. The abrupt growth of debonding resulted in a sudden drop of the load. After that, debonding continued to propagate gradually with an increase of the applied displacement. The load also gradually decreased while a stick slip phenomenon was observed in experiments. In this phase, debonding at the root of blade preceded.

The process of debonding growth, the debonding shape and the stiffness degradation of the specimen is complex, but the simulated results agreed with the experimental results.

4.2.2. Case 2: Transverse stiffened and bending and torsion loading. The process of debonding growth and the load–displacement relationship were similar to Case 1, but there were two different points. Debonding of the opposite side of the blade proceeded in the phase of debonding growth in the longitudinal direction. Another difference was that debonding occurred at the root of the blade near the free edge in the final phase of debonding. Both resulted from torsion and the influence of torsion was simulated successfully. The debonding growth and stiffness degradation were slower than experimental results. This implies that the mode III component of the energy release rate should be incorporated more correctly in the simulation.

4.2.3. Case 3: Parallel stiffened and bending loading. When the displacement reached 30 mm, debonding occurred at the root of the blade parallel to the clamped edge. This resulted in the abrupt drop of the load. Then, debonding propagated in the transverse direction of the stiffener according to the increase of the applied displacement, and the debonding growth brought the gradual decrease of the load. The stiffener was not useful in this case.

The process of debonding growth, the debonding shape and the load–displacement relationship were simulated successfully.

4.2.4. Case 4: Parallel stiffened and bending and torsion loading. When the displacement reached 20 mm, debonding occurred at the root of the blade near the loading point. Then, debonding propagated in the longitudinal direction with

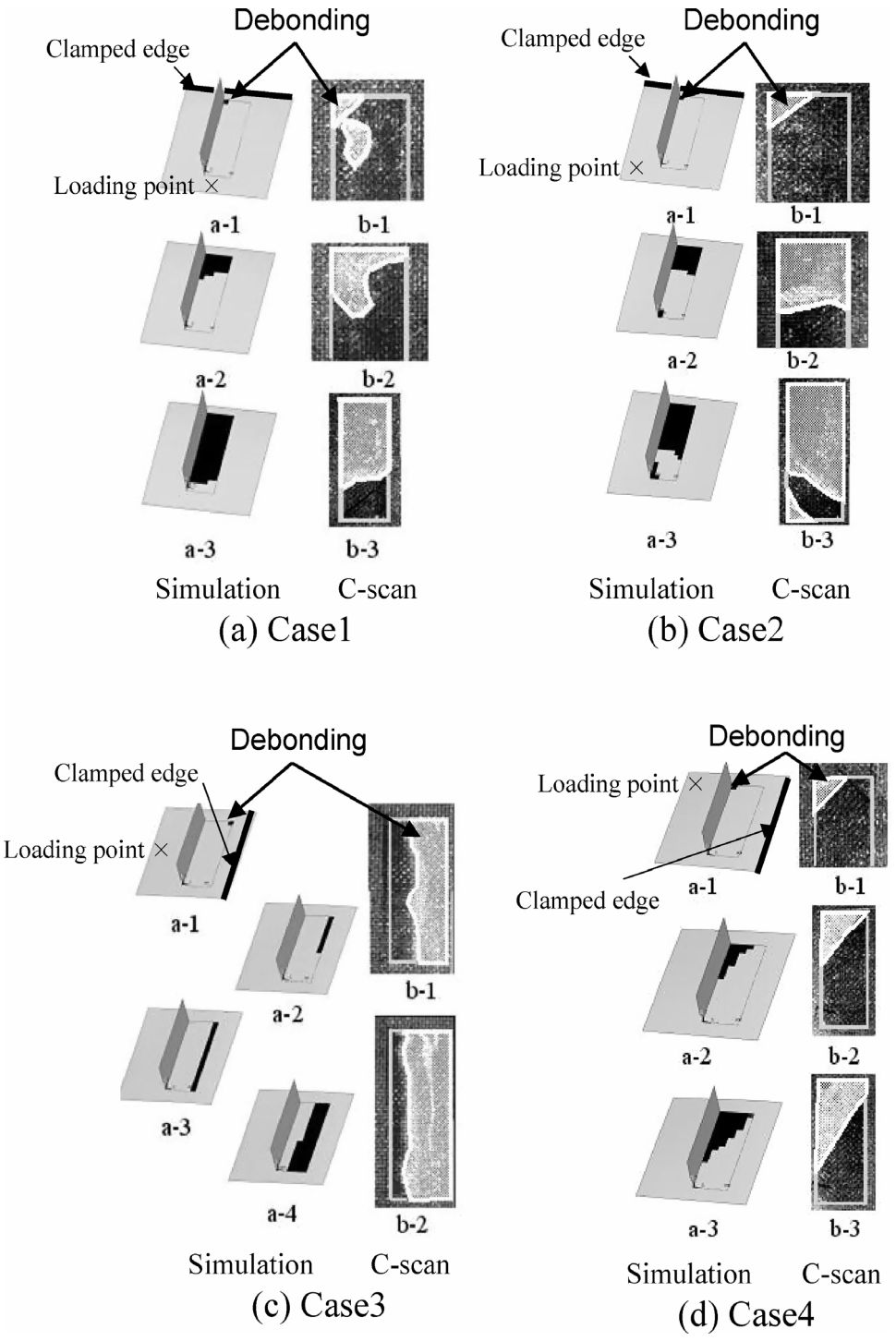

Figure 15. Simulated and observed debonding area.

the increase of the applied displacement, and the load gradually decreased. In the phase, debonding at the root of the blade preceded.

The process of debonding growth, the debonding shape and the load–displacement relationship were simulated successfully.

4.3. Influence of element size

The influence of element size was investigated. The analytical model in Fig. 13 was subdivided into a fine mesh: one element was subdivided into 4 elements. The four cases mentioned above were simulated by using the fine mesh. The processes of debonding growth and the debonding shapes were almost the same as in Fig. 15. The results indicate that the element size of Fig. 15 is fine enough to represent the debonding shape. This implies that an appropriate mesh size depends on the complexity of the debonding shape. The debonding shape of stiffeners is, however, not complex in general. Thus it is expected that the mesh size in Fig. 13 is generally acceptable.

In consequence of the similarity of debonding growth, the load–displacement relationships in the case of the fine mesh were similar to the results of the coarse mesh. Though the load of debonding onset was likely to be small if the mesh size was small, the mesh size did not affect the process of debonding growth, the debonding shape or the stiffness degradation. In the case of an abrupt debonding growth, a coarse mesh resulted in an excess load drop because the increment of debonding area was large when one node was decoupled. The excess load drop is on the safe side.

4.4. Conclusions regarding debonding of skin/stiffener structure

In this section, debonding of four skin/stiffener structures, which have a different orientation of the stiffener and a loading position, was simulated to demonstrate the feasibility of the proposed method. The process of debonding growth, the debonding shape and the load–displacement relationship were simulated successfully regardless of the orientation of the stiffener and the loading position.

5. GENERAL CONCLUSIONS

A simple simulation method for debonding of skin/stiffener structures was proposed, and debonding of beam specimens and skin/stiffener structures was simulated and compared with experimental results. The following conclusions were reached:

(1) Debonding of DCB and ELS specimens was simulated. The load–displacement relationship and the increment of debonding agreed with experimental results. It is shown that not only pure mode I but also mixed mode debonding can be simulated.

(2) Debonding of skin/stiffener structures was simulated to demonstrate the feasibility of the proposed method. The process of debonding growth, the debonding shape and the load–displacement relationship were simulated successfully.

REFERENCES

1. M. Kageyama, N. Arata, A. Yokoyama, H. Koiwai, S. Yoshida, M. Yoshida and T. Hoshi, Development of integrated composite main wing structure of XF-2, *Trans. JSCM* **28** (2), 80–84 (2002) (in Japanese).
2. J. T. Wang and I. S. Raju, Strain energy release rate formulae for skin-stiffener debond modeled with plate elements, *Eng. Fract. Mech.* **54** (2), 211–228 (1996).
3. J. Li, Flange delamination prediction in composite structures with ply waviness, *AIAA Journal* **38** (5), 893–897 (2000).
4. S. K. Satsangi, B. G. Prusty and C. Ray, First ply failure analysis of stiffened panels — a finite element approach, *Compos. Struct*. **51**, 73–81 (2001).
5. E. G. Falzon, G. A. O. Davies and E. Greenhaigh, Failure of thick-skinned stiffener runout sections loaded in uniaxial compression, *Compos. Struct*. **53**, 223–233 (2001).
6. Y. Shimamura, T. Inada, A. Todoroki, H. Kobayashi and Y. Nakamura, Inexpensive simulation of delamination growth in composite plates by using FEM with two-dimensional elements, *Trans. JSME* **64** (624A), 2046–2051 (1998) (in Japanese).
7. M. Zako and T. Tujikami, Development of simulation program for delamination of laminated composites, *J. Soc. Mater. Sci., Jpn*. **43** (489), 684–689 (1994) (in Japanese).
8. O. Majima and H. Suemasu, Nonlinear finite element analysis of multiple delamination propagation in composite laminates, *Trans. JSCM* **26** (6), 219–226 (2000) (in Japanese).
9. W. S. Chan, D. J. Chen and B. P. Wang, An efficient method to simulate one- and two-dimensional delamination growth in composite laminates, *J. Reinf. Plast. Compos.* **15**, 944–957 (1996).
10. S. Kamiya, H. Sekine and K. Yamada, Numerical approach to the interlaminar crack formation process in cross-ply laminates due to transverse loading, *Trans. JSME* **62** (593A), 18-25 (1996) (in Japanese).
11. S. Rinderknecht and B. Kröplin, A computational method for the analysis of delamination growth in composite plates, *Compos. Struct*. **64** (1-4), 359–374 (1997).
12. M. Arai, Y. Tateishi, T. Adachi and H. Matsumoto, Finite element analysis for damage propagation of CFRP laminated beam, *Trans. JSME* **64** (627), 2686–2693 (1998) (in Japanese).
13. E. A. Phillips, C. T. Herakovich and L. L. Graham, Damage development in composites with large stress gradients, *Compos. Sci. Technol.* **61** (15), 2169–2182 (2001).
14. I. S. Raju, Calculation of strain-energy release rates with higher order and singular finite elements, *Eng. Fract. Mech.* **28** (3), 251–274 (1987).
15. Y. Shimamura, A. Todoroki, H. Kobayashi and H. Nakamura, Effect of fracture mode on FRP damage simulation, *Trans. JSME* **62** (594A), 328–334 (1996) (in Japanese).
16. T. Miyoshi, M. Shiratori, M. Zako and S. Sakata, in: *Yugenyosohou*, p. 39. Jikkyo Shuppan, Tokyo (1994) (in Japanese).
17. D. R. J. Owen and E. Hinton, in: *Sosei no Yuugenyousohou*, p. 20. Science Press, Tokyo (1988) (in Japanese).
18. Japan Society for Composite Materials (Ed.), in: *Fukugouzairyo Katsuyo Jiten*, p. 591. Industrial Research Center of Japan, Inc.,Tokyo (2001) (in Japanese).
19. H. Suemasu, H. Hosoda and K. Nara, An experimental study of interlaminar toughness of satin woven fabric composite, *Trans. JSCM* **13** (5), 225–232 (1987) (in Japanese).